remote sensing

MDPI

Article

Study on the Erosion and Deposition Changes of Tidal Flat in Jiangsu Province Using ICESat-2 and Sentinel-2 Data

Kaizheng Wang [1], Huan Li [1,*], Nan Zhang [1], Jiabao Zhang [1], Xiaoyan Zhang [2] and Zheng Gong [1]

[1] College of Harbour, Coastal and Offshore Engineering, Hohai University, Nanjing 210098, China
[2] Shanghai Investigation, Design & Research Institute Co., Ltd., Shanghai 200335, China
* Correspondence: huanli@hhu.edu.cn

Abstract: The ecological dynamics of tidal flats are subject to continuous transformations attributed to the interplay of the tidal erosion and sedimentation processes. Accordingly, the realization of a dynamic monitoring system for tidal flats holds significant importance in facilitating the judicious utilization and safeguarding of tidal flats resources. In this study, an integrated methodology was implemented to monitor and assess the tidal flats in Jiangsu province. Specifically, a collection of five multispectral images from the Sentinel-2 satellite was acquired, coupled with data derived from the ICESat-2 satellite. Through the application of advanced techniques, including convolutional neural networks and machine learning algorithms, a comprehensive combined model for inverting tidal flats topography was developed. The accuracy disparity between various model combinations was meticulously evaluated, thereby enabling the acquisition of detailed topography information encompassing the entirety of Jiangsu's tidal flats for the year 2021. Comparative analysis against measured topographic data demonstrated that the overall accuracy of the combined model inversion surpassed 80%. Additionally, this study conducted an extensive investigation into the temporal evolution of tidal flats in Jiangsu by integrating data from 2008 to 2021, focusing particularly on the measured topography from 2008. Consequently, the study successfully delineated the various types of tidal flats present in Jiangsu and elucidated their corresponding evolutionary trends.

Keywords: tidal flats monitoring in Jiangsu Province; ICESat-2 data; Sentinel-2; tidal flats flushing and siltation evolution; convolutional neural network

Citation: Wang, K.; Li, H.; Zhang, N.; Zhang, J.; Zhang, X.; Gong, Z. Study on the Erosion and Deposition Changes of Tidal Flat in Jiangsu Province Using ICESat-2 and Sentinel-2 Data. *Remote Sens.* **2023**, *15*, 3598. https://doi.org/10.3390/rs15143598

Academic Editor: Javier Marcello

Received: 17 June 2023
Revised: 6 July 2023
Accepted: 12 July 2023
Published: 19 July 2023

1. Introduction

Tidal flats, as intertidal mudflats subjected to the ebb and flow of tides, play a crucial and multifaceted role in various coastal processes. They contribute significantly to carbon sequestration and storage, coastal protection, water purification, biodiversity enhancement, and socioeconomic development [1–3]. The Jiangsu Province in China hosts the most abundant and representative tidal flats resources, characterized by a total shoreline length of 888.945 km, securing its position as the leading province in China [4]. Nevertheless, the rapid pace of urbanization has imposed immense pressure on the development and utilization of tidal flats resources in Jiangsu, which has led to severe erosion issues [5,6]. Furthermore, natural calamities such as typhoons and storm surges have exacerbated the ecological vulnerability of these regions [7]. Monitoring changes in the ecological environment along coastal areas is of paramount importance to enhance the resilience of the coastal zone against natural disasters, safeguard the well-being and assets of individuals, and foster its sustainable development [8].

In the investigation of changes in the ecological environment along coastal areas, the elevation of tidal flats serves as a highly sensitive indicator of the external dynamic environment's erosion trends, providing valuable insights into future risks of tidal flats erosion. However, the silty tidal flats in Jiangsu exhibit substantial instability, erosion, and siltation variations [4], rendering traditional field survey methods impractical and cost-intensive for

long-term, dynamic, and large-scale monitoring of tidal flat evolution. In recent years, the advancement of active remote sensing technology has led to the emergence of airborne lidar systems capable of rapidly and accurately capturing three-dimensional spatial information of the ground and atmosphere [9,10]. A notable example is ICESat-2, a state-of-the-art laser altimetry satellite that diverges from previous full waveform lidars by eliminating the need to record waveforms to generate point clouds [11,12]. Instead, ICESat-2 directly detects individual photons, enabling the acquisition of vast amounts of photon point clouds and facilitating more precise and detailed section-level measurements. By synergistically integrating remote sensing images, it becomes possible to comprehensively grasp the evolution of tidal flats elevation across different periods. This combined approach not only enhances our understanding of the dynamic geomorphological processes influencing tidal flats but also addresses the limitations of relying solely on actual topographic data for remote sensing topographic inversion. Moreover, the integration of active remote sensing monitoring technology has the potential to overcome existing challenges and promote the widespread application of accurate and efficient topographic inversion techniques [13].

Previous approaches to remote sensing terrain inversion have primarily relied on empirical statistical methods, encompassing single-band models, multi-band models, and band ratio models [14–16]. In recent years, the utilization of machine learning techniques has gained substantial traction in remote sensing inversion due to its inherent strengths in addressing complex and nonlinear problems [17,18]. Nevertheless, as the volume of available observation data continues to grow, traditional machine learning algorithms face challenges in meeting the demands of large-scale data modeling [19]. The advent of deep learning theory, coupled with advancements in numerical computing resources, has sparked a renewed revolution in remote sensing inversion methods. Convolutional neural networks (CNNs) have emerged as a prominent exemplar of deep learning, exhibiting exceptional capabilities in nonlinear data processing. Consequently, CNNs have achieved remarkable success in practical applications, particularly within the engineering domain of remote sensing imagery analysis. By leveraging the nonlinear processing prowess of CNNs, researchers have achieved significant advancements in remote sensing inversion. These techniques have demonstrated their efficacy in tackling complex and intricate remote sensing problems by harnessing the vast potential of deep learning algorithms. This evolving landscape of remote sensing inversion methodologies not only opens new avenues for addressing the challenges of large-scale data modeling but also contributes to the broader spectrum of remote sensing applications [20–22].

However, the incorporation of multiple layers and nonlinear activation functions in convolutional neural network (CNN) models, although enabling the learning of intricate patterns and features, also introduces the risk of overemphasizing noise or minor variations present in the training set [23,24]. To address these challenges, numerous researchers have integrated CNNs with other machine learning algorithms to effectively mitigate the potential for model overfitting and enhance the generalization capabilities of the models. These integrated approaches have demonstrated significant success when combined with remote sensing technology in various domains such as wind field prediction, yield estimation, and land classification [25–27]. They have exhibited superior prediction performance and generally outperformed individual machine learning or CNN models in terms of overall accuracy. However, the application of such integrated methods in remote sensing terrain inversion remains relatively limited. Furthermore, most previous studies have focused solely on individual combinations of machine learning algorithms and CNNs, without explicitly exploring the variations in accuracy that different machine learning models may introduce when integrated into combined models. As a result, there is still a knowledge gap concerning the potential benefits and performance differences that can be achieved by leveraging diverse machine learning approaches in the context of remote sensing terrain inversion. To address this research gap and further enhance the accuracy and reliability of remote sensing terrain inversion, it is essential to explore and evaluate various machine learning algorithms in combination with CNNs. By conducting comprehensive analyses

and comparisons of different model configurations, we can gain valuable insights into the strengths and weaknesses of different approaches, leading to more informed decisions in designing effective and robust integrated models for remote sensing terrain inversion tasks.

The primary objective of this study is to enhance the convolutional neural network (CNN) approach to establish a refined tidal flats topographic inversion model. To achieve this goal, the study aims to address the following specific objectives: (1) Combine CNN with machine learning techniques to construct an optimized topographic inversion model for tidal flats, exploring different combinations of models and comparing their accuracy performance to identify the most effective approach; (2) Utilize ICESat-2 laser bathymetry data in conjunction with Sentinel-2 remote sensing images to derive comprehensive tidal flats topography information for the entire Jiangsu region in 2021 to obtain a more detailed and accurate characterization of the coastal topography; (3) Analyze the variation rules of the topography of the tidal flat in Jiangsu from 2008 to 2021 and determine the types and evolution trends of erosion and deposition in each bank segment in Jiangsu.

2. Materials and Methods

2.1. Research Area

The study area (Figure 1) encompasses the entirety of Jiangsu's tidal flats, situated in the central region of China's eastern coastline (31°33′~35°07′N). The area exhibits distinct geomorphological features, characterized by extensive muddy sediments, coastal wetlands, and saline lands [4].

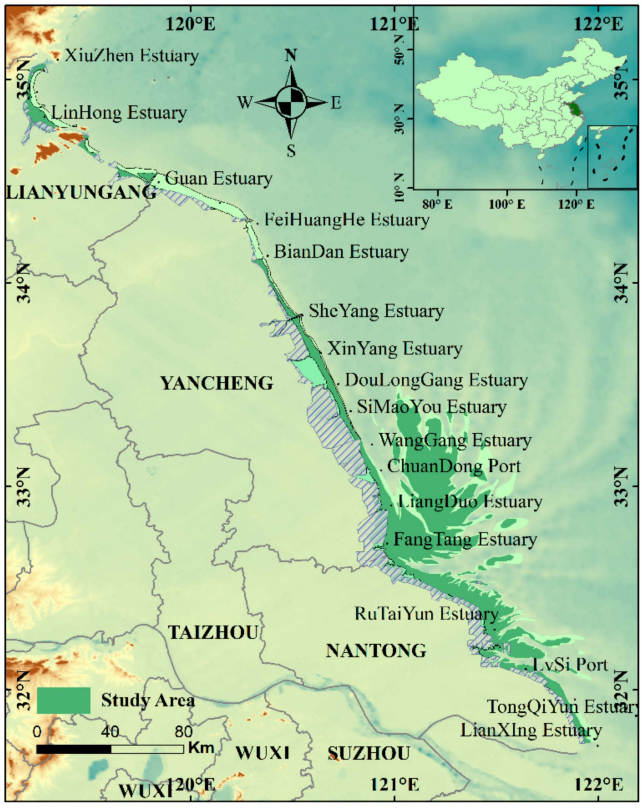

Figure 1. Schematic diagram of the location of the study area.

Hydrodynamics within the region is primarily influenced by the rotational tidal waves originating from the South Yellow Sea, as well as the advancing tidal waves from the East China Sea. Furthermore, the wave regime is predominantly composed of wind waves, creating a mixed wave system. The coastal zone is primarily characterized by a chalky-silt coastline, while the intertidal sediment types encompass a range of materials such as gravel, coarse sand, fine sand, very fine sand, chalky sand, sandy chalk, and clayey chalk. The

interplay of these sediments contributes to frequent fluctuations in shoreline erosion and sedimentation, providing an ideal setting for the investigation of tidal flat dynamics.

2.2. Data

2.2.1. Multispectral Remote Sensing Images

The remote sensing data utilized in this study were acquired from the European Space Agency's (ESA) Sentinel-2 multispectral imagery Level-2A products. These products are derived from two satellites, namely Sentinel-2A and Sentinel-2B, which operate in tandem to provide improved temporal resolution [28]. The Level-2A products have undergone preprocessing procedures, including radiometric and atmospheric corrections, based on the Level-1C products of atmospheric bottom reflectance images. These preprocessed data are readily applicable for various scientific and practical applications.

Given the extensive coverage required for this study area, a total of five cloud-free or minimally cloudy scenes of Sentinel-2 images were selected to ensure comprehensive coverage. The images were specifically chosen to capture low tide moments throughout the year, and selection criteria included low cloud cover, high data quality, and similarity in imaging moments. Among the 12 bands of Sentinel-2 images, B1, B9, and B10 exhibit a spatial resolution of 60 m, while B5, B6, and B7 have a spatial resolution of 20 m. The remaining bands possess a spatial resolution of 10 m. To achieve a consistent spatial resolution, we employed the Sentinel Application Platform (SNAP) to resample the Sentinel 2 images. The Bicubic interpolation method was employed for the resampling process, resulting in all the bands being adjusted to a spatial resolution of 10 m [29,30]. Further details can be found in Table 1, which provides specific information regarding the selected bands and their respective characteristics.

Table 1. Statistical table of Sentinel-2 remote sensing image information used.

ID	Figure Number	Date	Images Covered Area
1	50SQD	22 January 2021	XiuZhen to Abandoned-Yellow-River Estuary
2	51STT	24 March 2021	Abandoned-Yellow-River to XingYang Estuary
3	51STS	17 February 2021	XingYang to Si MaoYou Estuary
4	51SUS	18 January 2021	SiMao You to FangTang Estuary
5	51SUR	18 January 2021	FangTang to Tong QiYun Estuary

2.2.2. Laser Terrain Data

The laser topography data utilized in this study were obtained from the ICESat-2 satellite (Ice, Cloud, and Land Elevation Satellite-2). ICESat-2, launched by NASA in September 2018, represents a significant advancement in lidar satellite technology [11,12]. It introduces the novel capability of single-photon detection, enabling the more efficient and precise acquisition of Earth's elevation data. This satellite significantly improves the data acquisition rates compared to ICESat-1.

The ATL08 product, which is derived from the ATL03 data, a secondary product of ICESat-2, was utilized in this study. The ATL08 data undergoes adaptive nearest neighbor identification along the 10 km range of the orbital geolocation point cloud data [31]. This process generates the average topographic height within a 100 m range along the track direction. The product characteristics are illustrated in Figure 2. To conduct the research, ICESat-2 data were collected over the regional extent of Jiangsu tidal flats between June 2020 and June 2022. The spatial distribution of the data is presented in Figure 3a. The elevation data were measured in 2021, using the 1985 National Height Datum of China. Since this datum differs from the elevation datum, the WGS84 ellipsoid, used by ICESAT, a datum conversion was necessary. Therefore, it was necessary to convert the elevation data measured by ICESat-2 to the elevation based on the 1985 National Height Datum of China. The converted elevation was then employed to bulid the inversion model. This, in turn,

allowed us to evaluate the accuracy of the inversion model using the ground truth data collected in 2021.

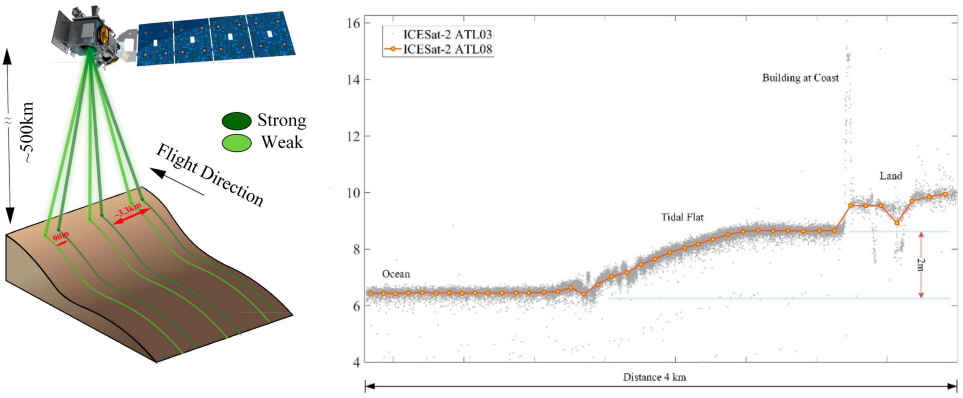

Figure 2. ICESat-2 ATL08 product laser topography data schematic.

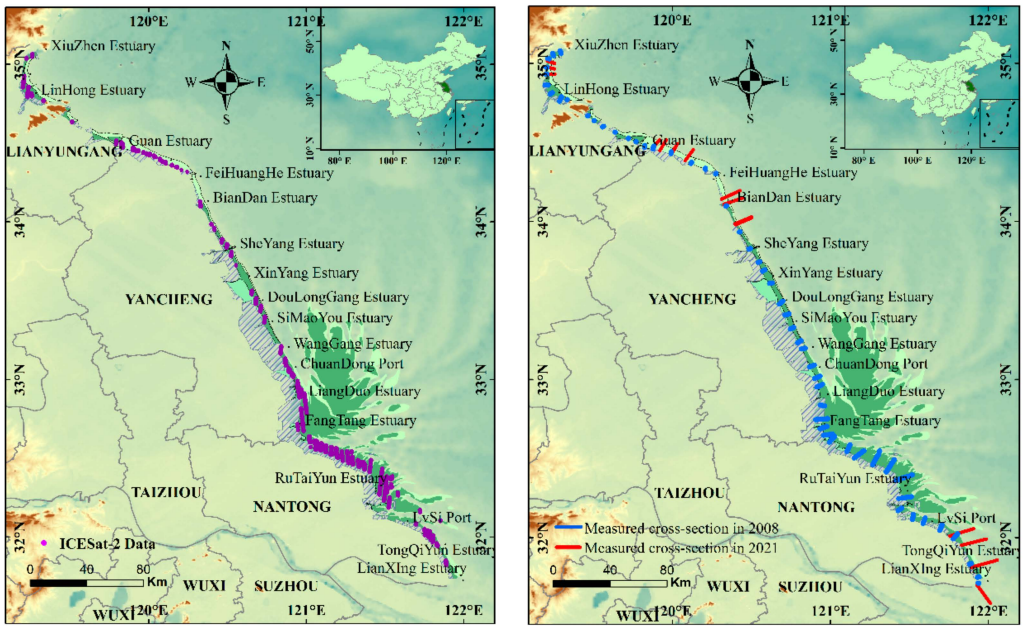

(**a**) (**b**)

Figure 3. Distribution of ICESat-2 and measured topographic data cross-sections. (**a**) ICESat-2 laser topography data distribution; (**b**) distribution of measured terrain data cross-sections.

2.2.3. Measured Terrain Data

The measured topographic data used in this study were obtained from two sources. The first source consists of 53 sections of elevation data along the Jiangsu coastal sections. The measured cross-sectional data of Jiangsu tidal flats, obtained through the 908 Special Project (China Offshore Marine Comprehensive Survey and Evaluation Special Project), were collected as the foundational data for topographic inversion in 2008. These data were employed in the establishment and accuracy verification of models.

2.3. Methods

This study utilizes ICESat-2 satellite ATL08 products and Sentinel-2 imagery to construct training samples for the inversion of tidal flat elevation in Jiangsu in 2021. By integrating convolutional neural networks and machine learning methods, a comprehensive optimization model for terrain inversion is developed. The accuracy differences between different model combinations are compared and evaluated.

2.3.1. Convolutional Neural Network

The relationship between tidal flat topography and remote sensing spectral reflectance is highly complex. The convolutional operation in convolutional neural networks effectively reduces the complexity of parameters and exhibits significant advantages in learning deep structures. The core concept in convolutional neural networks is the convolutional layer, which extracts features from input data by sliding a fixed-size filter. Subsequently, the pooling layer is utilized to reduce the size and parameter count of feature maps, thereby reducing the complexity of convolutional operations. After multiple rounds of convolution and pooling operations, the feature maps extracted by the convolutional and pooling layers are mapped to the final output using the weight coefficients of the fully connected layer [32].

2.3.2. Machine Learning

1. The Decision Tree model [33] is a supervised learning algorithm based on a tree-like structure. Firstly, it selects the most effective feature for classifying the current training data. Secondly, based on the selected feature, the training data are divided into multiple subsets, each containing the same feature values. Then, for each subset, steps 1 and 2 are recursively repeated until all data are assigned to leaf nodes. Afterward, unnecessary branches can be pruned to simplify and enhance the accuracy of the decision tree.
2. Backpropagation (BP) neural network [34] is based on the idea of dividing the learning process into two stages. The first stage is the forward propagation process, where input information is processed through hidden layers, and the actual output values of each unit are computed. The second stage is the backward propagation process. If the desired output is not obtained at the output layer, the difference between the actual output and the desired output (i.e., the error) is calculated layer by layer. Based on this difference, the weights are adjusted to correct the connections between layers in a backward manner.
3. Gaussian Process Regression (GPR) [35] assumes that the variables in terrain prediction follow a Gaussian distribution and represents the covariance structure between input variables as a covariance matrix. By using training data, the model parameters, i.e., the elements of the covariance matrix, are updated. This allows for the prediction of the expected value and variance in the output terrain variable. The prediction results are then used to calculate confidence intervals, enabling Gaussian Process Regression to be implemented.

2.3.3. Combinatorial Model

This paper proposes a model combination method that combines convolutional neural networks with other machine learning algorithms to effectively improve model accuracy and generalization ability. Based on the MATLAB packages, including Regression-Trees, Neural-Networks, Gaussian-Process-Regression, and Pretrained-Convolutional-Neural-Networks, we established inversion models to obtain the topography of tidal flats. The sample dataset is divided into three categories: 60% for the training set, 20% for the test set, and 20% for the validation set. The training of the convolutional neural network and other machine learning models will use the training set data, and the optimization of weights for the convolutional neural network and machine learning models will use the test set. All subsequent accuracy validations will be conducted using the validation set.

Since the test set and validation set have the same proportion and come from the same data source, optimizing the model based on the test set data often leads to good accuracy results on the validation data as well. In addition, convolutional neural networks and machine learning models have different feature recognition capabilities, and individual models may produce anomalous values. However, a combined model can consider the results of each model's inversion and effectively prevent the occurrence of outlier values.

As a result, the overall accuracy of the combined model is often higher than that of a single model.

In the specific methodology, after training the convolutional neural network and the machine learning models, the weights for the outputs of the convolutional neural network and a specific machine learning model are determined based on the test set data. In this study, we iterate through the range of 0 to 1 with a step size of 0.001 for the weights of the convolutional neural network outputs. Using this weight value, the weights for the machine learning models are determined (the sum of all model weights is 1). We test 100 combinations of weights on the test set and select the parameters that yield the highest validation accuracy. The weight values that are numerically closest to 0.5 are chosen to prevent the model weights from being excessively close to 1 or 0. The prediction output of the combined model is obtained by taking the sum of the product of each model's prediction and its corresponding weight, as shown in Figure 4.

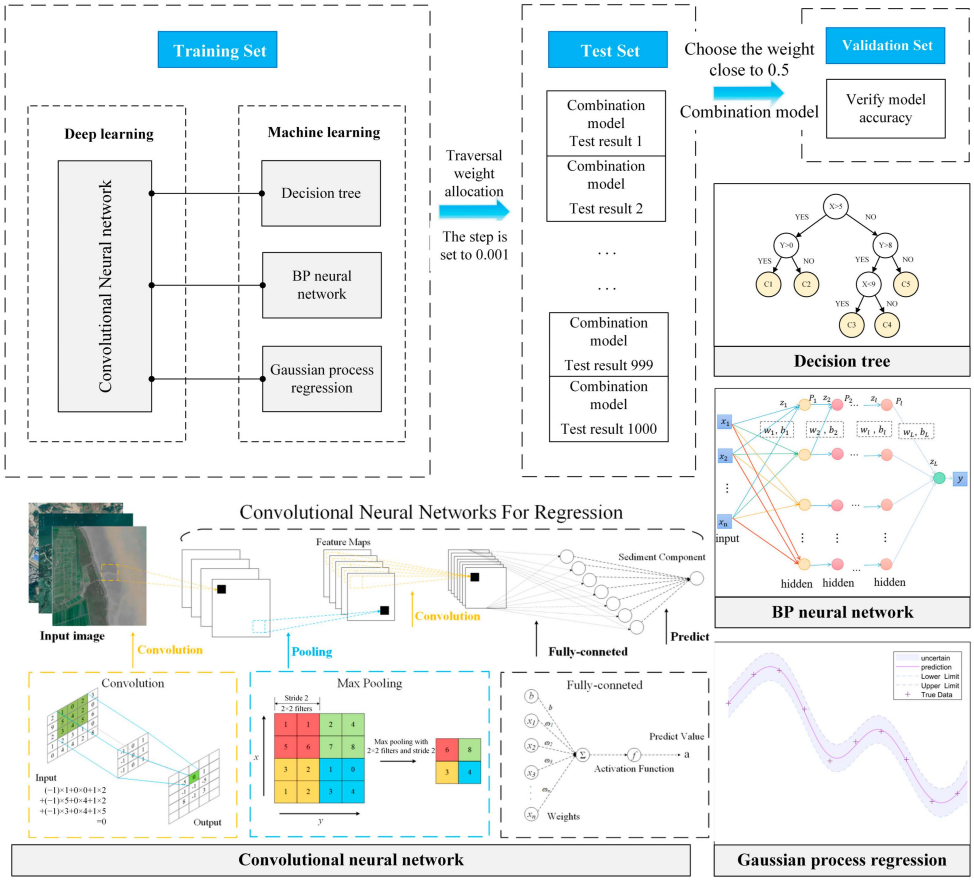

Figure 4. Schematic diagram of the optimization method of the combined tidal flats topography inversion model.

3. Results

3.1. Model Accuracy

Based on the ICESat-2 ATL08 data from June 2020 to June 2022 and the five scenes of Sentinel-2 data, combination models based on a Convolutional Neural Network (CNN) with Decision Tree (TREE), Backpropagation Neural Network (BP), and Gaussian Process Regression (GPR) are constructed for each image. Due to the smaller coverage of data in the second and third scenes compared to the first, fourth, and fifth scenes, the data from the second and third scenes are merged and modeled together. The average absolute error (MAE), root mean square error (RMSE), correlation coefficient (R), and coefficient of determination (R^2) are calculated for each regional model, as shown in Table 2.

Table 2. Validation of topographic inversion model accuracy for 2021 ICESat-2 ATL08 data and 5view Sentinel-2 data. (Bolded: Final Selected Model).

Area	Model	RMSE(m)	MAE	R	R^2	Weights	
						CNN	ML
Scene 1	CNN	0.43	0.231	0.919	0.845		
	TREE	0.58	0.342	0.850	0.723		
	CNN-TREE	0.44	0.260	0.918	0.844	0.478	0.522
	BP	0.67	0.441	0.795	0.632		
	CNN-BP	0.49	0.312	0.895	0.801	0.480	0.520
	GPR	0.41	0.206	0.931	0.867		
	CNN-GPR	**0.40**	**0.209**	**0.933**	**0.870**	**0.550**	**0.450**
Scene 2 & Scene 3	CNN	0.58	0.342	0.883	0.779		
	TREE	0.75	0.520	0.793	0.629		
	CNN-TREE	**0.55**	**0.371**	**0.890**	**0.792**	**0.458**	**0.542**
	BP	0.90	0.652	0.685	0.469		
	CNN-BP	0.62	0.439	0.859	0.738	0.499	0.501
	GPR	0.74	0.331	0.815	0.664		
	CNN-GPR	0.59	0.310	0.877	0.770	0.523	0.477
Scene 4	CNN	0.42	0.305	0.797	0.636		
	TREE	0.48	0.327	0.703	0.494		
	CNN-TREE	0.41	0.287	0.794	0.630	0.453	0.547
	BP	0.50	0.352	0.699	0.488		
	CNN-BP	0.41	0.300	0.787	0.620	0.414	0.586
	GPR	0.41	0.206	0.807	0.650		
	CNN-GPR	**0.36**	**0.238**	**0.845**	**0.714**	**0.495**	**0.505**
Scene 5	CNN	0.39	0.253	0.915	0.837		
	TREE	0.42	0.223	0.906	0.820		
	CNN-TREE	0.35	0.227	0.933	0.871	0.824	0.176
	BP	0.48	0.309	0.871	0.759		
	CNN-BP	0.40	0.269	0.911	0.829	0.412	0.588
	GPR	0.34	0.231	0.936	0.877		
	CNN-GPR	**0.34**	**0.228**	**0.936**	**0.876**	**0.414**	**0.587**

Based on the comparison of the models mentioned above, the combination models generally exhibit improved accuracy compared to single Convolutional Neural Network (CNN) models or individual machine learning methods. The RMSE is reduced by approximately 0.04 m, resulting in an error reduction of about 5% to 10%. Among the combination models, the CNN-Gaussian Process Regression (CNN-GPR) and CNN-Decision Tree (CNN-TREE) models demonstrate the highest overall inversion accuracy, with an average RMSE of approximately 0.44 m.

3.2. Model Accuracy by Measured Data

To further understand the accuracy of using ICESat-2 data combined with multispectral satellite imagery to infer tidal flat elevation, field measurements were collected along the coast of Jiangsu in 2021, comprising a total of 15 transects. The distribution of these transects is shown in Figure 3b. The predicted values obtained from the combined model using the measured transect points were compared with the actual measured data. Detailed comparisons for each transect are presented in Figure 5. The maximum RMSE is 0.65 m (Transect 7), while the minimum RMSE is 0.09 m (Transect 9).

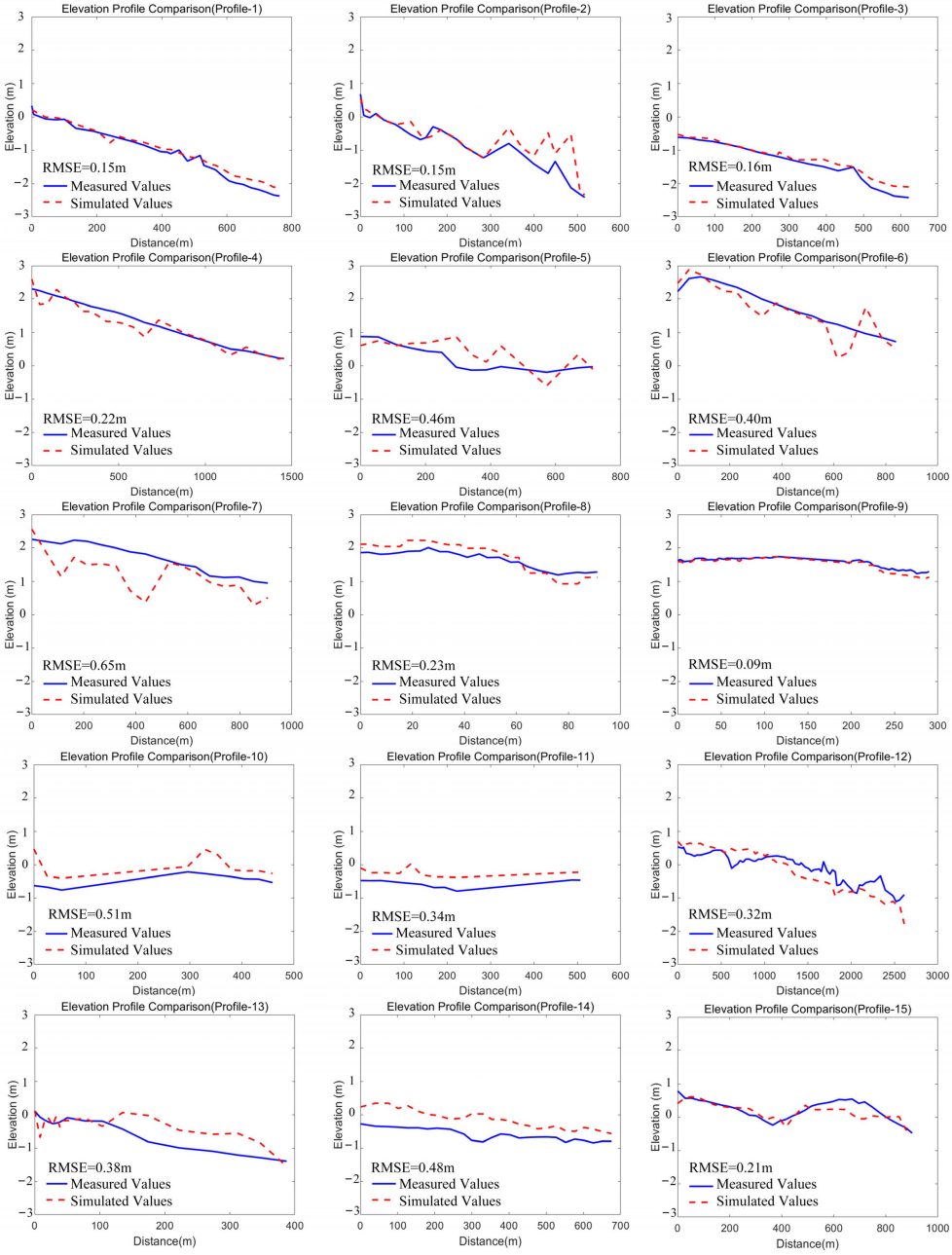

Figure 5. Comparison of simulated and measured values for the 2021 cross-section (Dist = 0 m indicates the starting point of the section; please note the varying X-axis limits in each graph).

Traditional field survey methods provide accurate terrain data but are limited in terms of obtaining sufficient data coverage. By incorporating ICESat-2 laser altimetry data and synergizing with Sentinel-2 imagery, a combined model using convolutional neural networks (CNN) and general machine learning methods were employed for large-scale terrain inversion. The average RMSE achieved through this approach was approximately 0.2 m. This method enables the acquisition of extensive terrain information without relying solely on field measurements, utilizing remote sensing data instead.

During the terrain inversion process, a challenge was encountered due to the turbidity of the water bodies in Jiangsu. The laser signals from ICESat-2 had difficulty penetrating through the water, especially when the tidal flats were submerged during high tide. As a result, the terrain inversion errors were primarily concentrated in the high tidal flat areas. If it becomes possible to acquire accurate terrain data for the high tidal flat regions,

it would contribute to further improvements in the accuracy of terrain inversion using ICESat-2 data.

3.3. Inversion Results

The optimal models for terrain inversion, as determined in Section 3.1, were used to perform the terrain inversion for Jiangsu tidal flats in 2021. The resulting elevation data for the tidal flats in Jiangsu are presented in Figure 6. The elevation reference used in this study is based on the 1985 National Height Datum.

As shown in Figure 6a, the tidal flats area in the northern part of Jiangsu, from the Xiuzhen River Estuary to the Linhong River Estuary, exhibits an elevation ranging from −2.5 m to 0.5 m. The southern area of the Xiuzhen River Estuary shows local sedimentation, which could be attributed to the presence of structures such as breakwaters and embankments, as observed from satellite imagery. These structures have caused sediment accumulation, resulting in localized sedimentation in the southern tidal flats area of the Xiuzhen River Estuary. In Figure 6b, the tidal flats area from the Guan River Estuary to the Abandoned-Yellow-River River Estuary in 2021 shows an elevation range of approximately −0.5 m to 2.5 m. There is more sedimentation in the upper part of the area compared to the lower part, and the overall slope exhibits a steeper trend. At the river mouth, there are channel regulation projects and measures promoting sediment accumulation, such as the introduction of Spartina alterniflora, a type of grass. There is a higher accumulation of sediment on the landward side.

As shown in Figure 6c, the tidal flats area in the southern part of Jiangsu, from the Biandan River Estuary to the Sheyang River Estuary, exhibits an elevation range of approximately −0.5 m to 2.0 m. There is a steep slope in the northern part of the Sheyang River Estuary, which is located between the two river mouths. The tidal flats in this section are almost submerged by water, indicating an erosional state. Only partial sedimentation can be observed at the river mouth. In Figure 6d, the tidal flats area from the Sheyang River Estuary to the Liangduo River Estuary exhibits an elevation range of approximately −0.5 m to 2.0 m in 2021. The area has been influenced by reclamation activities, resulting in more sediment accumulation on the landward side and slight sedimentation on the seaward side. Overall, the area shows a sedimentation state with some sections exhibiting erosion.

As described in Figure 6e, the area from the Liangli River Estuary to Yaowang Port in southern Jiangsu Province exhibits an elevation range of approximately −0.5 m to 2.0 m in 2021. This area is located at the convergence of two major tidal wave systems, resulting in complex tidal dynamics and a higher number of upstream river inlets. Consequently, the area features complex topography with a well-developed tidal channel system. Overall, there is a tendency towards siltation with some local scouring. In Figure 6f, the area from Yaowang Port to Lianxing Port shows an elevation range of approximately −1.5 m to 1.0 m in 2021. The tidal flats in this section experience erosion on the seaward side, while there is slight sedimentation occurring at the corner of the polder, Ding dam, and breakwater.

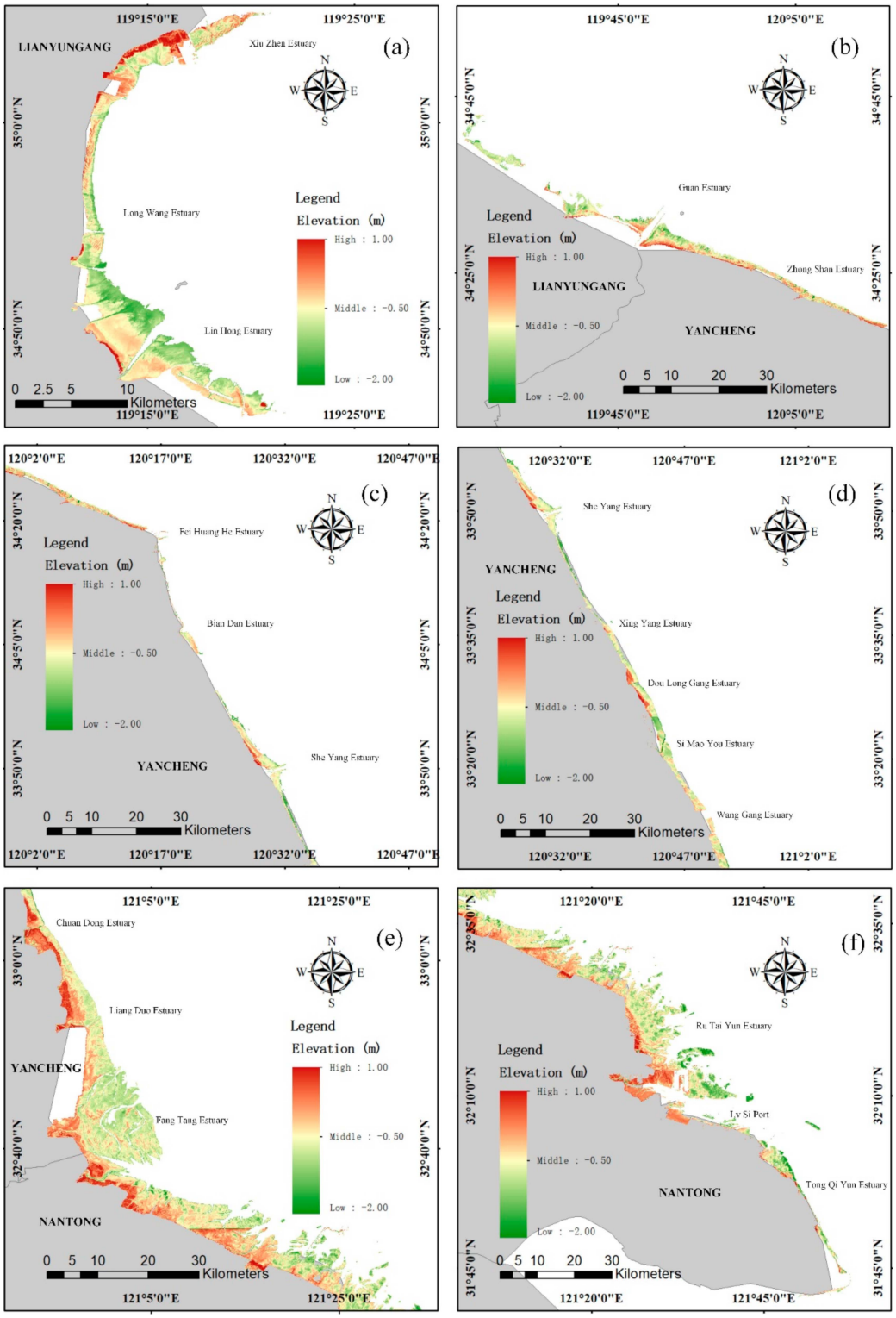

Figure 6. Inverse map of Jiangsu tidal flats elevation in 2021. (**a**) From the Xiuzhen River Estuary to the Linhong River Estuary (**b**) From the Guan River Estuary to the Abandoned-Yellow-River River Estuary (**c**) From the Biandan River Estuary to the Sheyang River Estuary (**d**) From the Sheyang River Estuary to the Liangduo River Estuary (**e**) From the Liangli River Estuary to Yaowang Port (**f**) From Yaowang Port to Lianxing Port.

3.4. Analysis of Erosion and Deposition Pattern

According to the comparison between the measured cross-sectional data from 2008 and the terrain retrieval from ICESat-2 in 2021, the elevation changes in each cross-section from 2008 to 2021 were calculated. By integrating remote sensing image observations, the variations in sedimentation and erosion in the tidal flats of Jiangsu were analyzed, and the classification of sedimentation and erosion types along the coast was performed. Based on the positive and negative values as well as the magnitude of elevation changes for each cross-section, the coastal areas of Jiangsu can be roughly divided into 15 regions. The sedimentation and erosion patterns in each coastal region are shown in Figure 7.

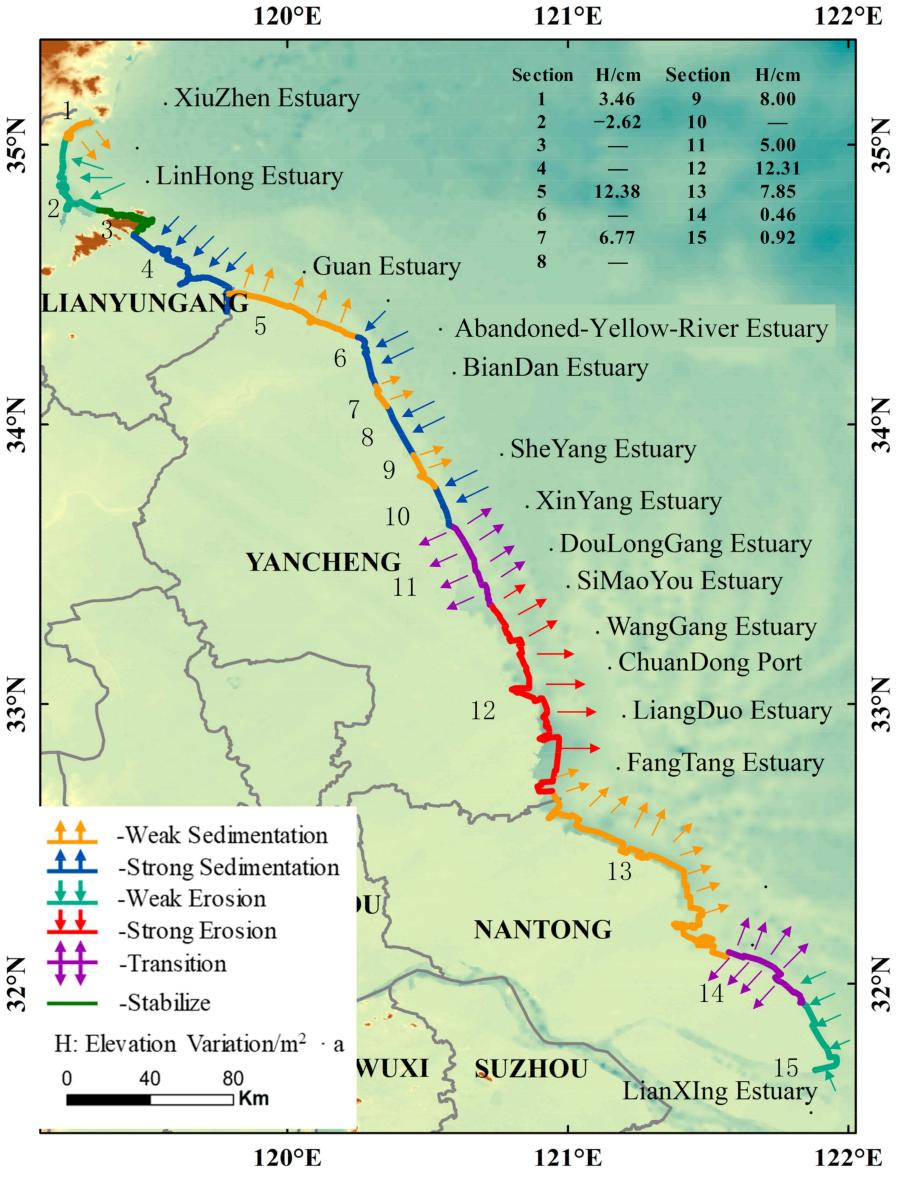

Figure 7. Analysis of the evolution of flushing and siltation. 1–15 represent different segments of the coastal area of Jiangsu, among which 1: From Xiuzhen Estuary to Longwang Estuary; 2: From Longwang Estuary to Linhong Estuary; 3: From Linhong Estuary to Shaoxiang Estuary; 4: From Shaoxiang Estuary to Guan Estuary; 5: From Guan Estuary to Abandoned-Yellow-River Estuary; 6: From Feihuanghe Estuary to Biandan Estuary; 7: Biandan Estuary; 8: From Biandan Estuary to Sheyang Estuary; 9: Sheyang Estuary; 10: From Sheyang Estuary to Xinyang Estuary; 11: From Xinyang Estuary to Simaoyou Estuary; 12: From Simaoyou Estuary to Fangtang Estuary; 13: From Fangtang Estuary to Lusi Port; 14: From Lusi Port to Tongqi Port; 15: From Tongqi Port to Lianxing Port.

1. The vicinity of the Xiu Zhen River estuary (Segment 1) is classified as a weak sedimentation zone, with an average annual elevation increase of 3.46 cm. From the south of the Xiu Zhen River estuary to the south of the Lin Hong River estuary (Segment 2), it is classified as a weak erosion zone, with an average annual elevation decrease of 2.62 cm. From the south of the Lin Hong River estuary to the Shao Xiang River estuary (Segment 3), it is categorized as a bedrock zone, indicating a stable shoreline with no significant changes in a tidal flat area and elevation. From the Shao Xiang River estuary to the Guan River estuary (Segment 4), it is classified as a strong erosion zone. From the Guan River estuary to the Abandoned-Yellow-River estuary (Segment 5), it is identified as a weak sedimentation zone, with an average annual elevation increase of 12.38 cm.
2. From the Abandoned-Yellow-River estuary to the Xin Yang River estuary (Segments 6–10), it is classified as a strong erosion zone with localized weak sedimentation (Bian Dan River estuary, Sheyang River estuary). The average annual elevation increase at the Bian Dan River estuary is 6.77 cm, and at the Sheyang River estuary is 8.00 cm. From the Xin Yang River estuary to the Si Mao You River estuary (Segment 11), it is considered a transitional zone, with an average annual elevation increase of 5.0 cm. From the Si Mao You River estuary to the Fang Tang River estuary (Segment 12), it is classified as a strong sedimentation zone, with an average annual elevation increase of 12.31 cm.
3. From the Fang Tang River estuary to Lu Si Port (Segment 13), it is categorized as a weak sedimentation zone, with an average annual elevation increase of 7.85 cm. From Lu Si Port to Tong Qi Yun Port (Segment 14), it is identified as a transitional zone, with a relatively small elevation increase of 0.46 cm. From Tong Qi Yun Port to Lian Xing Port (Segment 15), it is classified as a strong erosion zone, with an average annual elevation increase of 0.92 cm.

4. Discussion

The factors influencing the sedimentation dynamics of tidal flats in Jiangsu are highly complex. Generally, the key determinants of tidal flat development or erosion include sediment sources, hydrodynamic conditions, and anthropogenic influences [36–38]. Along the Jiangsu coast, an abundant supply of fine-grained sediments leads to their accumulation under tidal action, which results in wave energy dissipation and reduced wave impact. In certain small bays with weaker tidal forces, this process leads to the formation of small-scale tidal flats [39]. The Xiu Zhen River estuarine area (segment 1) is characterized as a weakly sedimented segment, likely due to the aforementioned reasons.

Furthermore, when the supply of sediment is sufficient, tidal flats exhibit strong accretion characteristics. The abundant silt and clay derived from the Yellow River and the modern Yangtze River are major sediment sources for tidal flats in Jiangsu [40]. We have found that the composition of large-scale sandy shoals in the area from the Si Mao You River mouth to the Fang Tang River mouth (segment 12) and from the Fang Tang River mouth to the Lv Si Port (segment 13) is primarily formed by the sediment supply from these two rivers.

Severe tidal flat erosion occurs when the hydrodynamic conditions are stronger than the sediment supply intensity. Some sediments can be trapped within river estuaries or bays. If local sand bars block the alongshore sediment transport, sediment loss near the coastline can lead to retreat [41]. This may explain the formation mechanism of the weakly eroded segment from the south of the Xiu Zhen River mouth to the Linhong River mouth (segment 2). Additionally, the segments from the south of the Linhong River mouth to the Shaoxiang River mouth (segment 3) and from the Shaoxiang River mouth to the Guan River mouth (segment 4) are predominantly composed of bedrock, which is likely due to the combined effect of insufficient sediment supply and persistent erosion.

Furthermore, human activities are also contributing factors to tidal flat evolution [38]. In the segment from the GuanHe River mouth to the north of the Abandoned-Yellow-River

mouth (segment 5), sediment accumulation occurs due to the presence of a guide levee at the Guan River mouth. The segments from the Abandoned-Yellow-River mouth to the Xin Yang River mouth (segments 6–10) are characterized as strongly eroded segments.

The geomorphological pattern of the tidal flats can be attributed to both the asymmetric distribution of current activity resulting from tidal bulge and the uneven sediment supply. Tao [42] built an idealized morphodynamic model for the hydrodynamic analysis of the South Yellow Sea region in the Jiangsu coastal region, which overlaps with the area of our study. The formation and maintenance of the tidal flats in this region are primarily driven by the tidal regime. In general, the changes in sedimentation patterns on tidal flats are governed by the combined influence of external hydrodynamics and sediment supply sources. The interplay between these factors in a relatively balanced environment often leads to the development of characteristic features in transitional segments. The segments from the Xin Yang River mouth to the Si Mao You River mouth (segment 11) and from LvSi Port to the Tongqi Canal mouth (segment 14) are located on either side of the Mao You River mouth to LvSi Port (segments 12 and 13). They are transitional segments where some cross-sections show accretion in high-tide areas and erosion in low-tide areas, and the slopes become steeper [39].

It should be acknowledged that changes in elevation can be attributed to various processes beyond erosion and deposition, including land subsidence and expansion. However, their influence on elevation variation is relatively small in terms of the observed scale. Gong [43] conducted an extensive long-term in situ investigation in the Jiangsu coastal region, which overlaps with the area of our study. Their findings indicate that subsurface processes, such as soil subsidence and expansion, have a significant impact on the bed level of the upper intertidal flat where salt marshes are present. Nonetheless, it is important to emphasize that our research specifically focuses on bare tidal flats, and therefore we have not accounted for the contribution of land subsidence in our analysis.

5. Conclusions

This study focuses on the entire tidal flat region of Jiangsu Province as the study area. ICESat-2 data and field-measured topographic data are used as the data sources, along with Sentinel-2 imagery. A combination model consisting of convolutional neural networks and three machine learning methods (Decision Tree model, BP neural network, and GPR) is employed for tidal flat topography inversion. The research findings are as follows:

1. This study focuses on the entirety of the tidal flat region within Jiangsu Province as the designated study area. The data sources utilized in this research include ICESat-2 data, field-measured topographic data, and Sentinel-2 imagery. To achieve tidal flat topography inversion, a hybrid model comprising convolutional neural networks (CNN) and three machine learning methods (Decision Tree model, BP neural network, and GPR) is employed. The key findings of this study are as follows: The utilization of ICESat-2 laser bathymetry data in conjunction with Sentinel-2 multispectral remote sensing images enables the development of a remote sensing inversion combination model based on CNN and machine learning methods (Decision Tree model, BP neural network, and GPR), resulting in a highly accurate large-scale tidal flat terrain inversion method.
2. This paper obtains the topographic information of tidal flats in Jiangsu for the years 2008 and 2021. A comparative analysis is conducted to examine the changes in tidal flat area and intertidal terrain across different historical periods. Furthermore, an in-depth investigation is conducted to analyze the erosion and sedimentation characteristics of tidal flats in Jiangsu.

Author Contributions: Conceptualization, H.L. and K.W.; methodology, K.W. and N.Z.; software, N.Z.; validation, H.L., K.W. and N.Z.; formal analysis, K.W. and J.Z.; investigation, X.Z.; data curation, K.W.; writing—original draft preparation, K.W. and J.Z.; writing—review and editing, N.Z., X.Z. and H.L.; visualization, N.Z. and X.Z.; supervision, H.L.; project administration, H.L. and Z.G.;

funding acquisition, H.L., J.Z. and Z.G. All authors have read and agreed to the published version of the manuscript.

Funding: This research was funded in part by National Key R&D Program of China (Grant No. 2022YFC3106204), in part by the Marine Science and Technology Innovation Project of Jiangsu Province (Grant No. JSZRHYKJ202214), and in part by the Carbon Peak Carbon Neutral Science and Technology Innovation Projects of Jiangsu Province (Grant No. BK20220020).

Data Availability Statement: The Sentinel-2 data used in this study are available on the ESA Copernicus Data Centre (https://scihub.copernicus.eu/dhus/#/home, accessed on 21 January 2023). Researchers can access the ICESat-2 data free of charge through the Open Altimetry website (https://openaltimetry.org/data/icesat2, accessed on 15 January 2023).

Acknowledgments: We thank the NSIDC for providing the ICESat-2 products and ESA Copernicus Data Centre for providing the Sentinel-2 data.

Conflicts of Interest: All authors disclosed no relevant relationships.

References

1. Bauer, J.E.; Cai, W.J.; Raymond, P.A.; Bianchi, T.S.; Hopkinson, C.S.; Regnier, P.A. The changing carbon cycle of the coastal ocean. *Nature* **2013**, *504*, 61–70. [CrossRef] [PubMed]
2. Pendleton, L.; Donato, D.C.; Murray, B.C.; Crooks, S.; Jenkins, W.A.; Sifleet, S.; Craft, C.; Fourqurean, J.W.; Kauffman, J.B.; Marbà, N.; et al. Estimating global "blue carbon" emissions from conversion and degradation of vegetated coastal ecosystems. *PLoS ONE* **2012**, *7*, e43542. [CrossRef] [PubMed]
3. Lotze, H.K.; Lenihan, H.S.; Bourque, B.J.; Bradbury, R.H.; Cooke, R.G.; Kay, M.C.; Kidwell, S.M.; Kirby, M.X.; Peterson, C.H.; Jackson, J.B.C. Depletion, Degradation, and Recovery Potential of Estuaries and Coastal Seas. *Science* **2006**, *312*, 1806–1809. [CrossRef] [PubMed]
4. Dai, W.; Li, H.; Gong, Z.; Zhang, C.; Zhou, Z. Application of unmanned aerial vehicle technology in geomorphological evolution of tidal flat. *Adv. Water Sci.* **2019**, *30*, 359–372. [CrossRef]
5. Halpern, B.S.; Walbridge, S.; Selkoe, K.A.; Kappel, C.V.; Micheli, F.; D'Agrosa, C.; Bruno, J.F.; Casey, K.S.; Ebert, C.; Fox, H.E.; et al. A Global Map of Human Impact on Marine Ecosystems. *Science* **2008**, *319*, 948–952. [CrossRef] [PubMed]
6. Yu, W.-J.; Zou, X.-Q. The Research on the Farmer Households' Economic Behavior and Sustainable Utilization Issues in Tidal Flat of Jiangsu Province. *Adv. Sci. Lett.* **2013**, *19*, 1819–1822. [CrossRef]
7. Hoegh-Guldberg, O.; Mumby, P.J.; Hooten, A.J.; Steneck, R.S.; Greenfield, P.; Gomez, E.; Harvell, C.D.; Sale, P.F.; Edwards, A.J.; Caldeira, K.; et al. Coral reefs under rapid climate change and ocean acidification. *Science* **2007**, *318*, 1737–1742. [CrossRef]
8. Liu, J.; Kuang, W.; Zhang, Z.; Xu, X.; Qin, Y.; Ning, J.; Zhou, W.; Zhang, S.; Li, R.; Yan, C.; et al. Spatiotemporal characteristics, patterns, and causes of land-use changes in China since the late 1980s. *J. Geogr. Sci.* **2014**, *24*, 195–210. [CrossRef]
9. Kutser, T.; Hedley, J.; Giardino, C.; Roelfsema, C.; Brando, V.E. Remote sensing of shallow waters—A 50 year retrospective and future directions. *Remote Sens. Environ.* **2020**, *240*, 111619. [CrossRef]
10. Goetz, A.F.; Vane, G.; Solomon, J.E.; Rock, B.N. Imaging spectrometry for Earth remote sensing. *Science* **1985**, *228*, 1147–1153. [CrossRef]
11. Markus, T.; Neumann, T.; Martino, A.; Abdalati, W.; Brunt, K.; Csatho, B.; Farrell, S.; Fricker, H.; Gardner, A.; Harding, D.; et al. The Ice, Cloud, and land Elevation Satellite-2 (ICESat-2): Science requirements, concept, and implementation. *Remote Sens. Environ.* **2017**, *190*, 260–273. [CrossRef]
12. Wang, B.; Ma, Y.; Zhang, J.; Zhang, H.; Zhu, H.; Leng, Z.; Zhang, X.; Cui, A. A noise removal algorithm based on adaptive elevation difference thresholding for ICESat-2 photon-counting data. *Int. J. Appl. Earth Obs. Geoinf.* **2023**, *117*, 103207. [CrossRef]
13. Li, W.; Niu, Z.; Shang, R.; Qin, Y.; Wang, L.; Chen, H. High-resolution mapping of forest canopy height using machine learning by coupling ICESat-2 LiDAR with Sentinel-1, Sentinel-2 and Landsat-8 data. *Int. J. Appl. Earth Obs. Geoinf.* **2020**, *92*, 102163. [CrossRef]
14. Carnes, M.R.; Teague, W.J.; Mitchell, J.L. Inference of subsurface thermohaline structure from fields measurable by satellite. *J. Atmos. Ocean. Technol.* **1994**, *11*, 551–566. [CrossRef]
15. Fox, D.N.; Teague, W.J.; Barron, C.N.; Carnes, M.R.; Lee, C.M. The Modular Ocean Data Assimilation System (MODAS). *J. Atmos. Ocean. Technol.* **2002**, *19*, 240–252. [CrossRef]
16. Nardelli, B.B.; Santolert, R. Reconstructing Synthetic Profiles from Surface Data. *J. Atmos. Ocean. Technol.* **2004**, *21*, 693–703. [CrossRef]
17. Su, H.; Yang, X.; Lu, W.; Yan, X. Estimating Subsurface Thermohaline Structure of the Global Ocean Using Surface Remote Sensing Observations. *Remote Sens.* **2019**, *11*, 1598. [CrossRef]
18. Lary, D.J.; Alavi, A.H.; Gandomi, A.H.; Walker, A.L. Machine learning in geosciences and remote sensing. *Geosci. Front.* **2016**, *7*, 3–10. [CrossRef]
19. Reichstein, M.; Camps-Valls, G.; Stevens, B.; Jung, M.; Denzler, J.; Carvalhais, N.; Prabhat. Deep learning and process understanding for data-driven Earth system science. *Nature* **2019**, *566*, 195–204. [CrossRef]

20. Hoeser, T.; Kuenzer, C. Object Detection and Image Segmentation with Deep Learning on Earth Observation Data: A Review-Part I: Evolution and Recent Trends. *Remote Sens.* **2020**, *12*, 1667. [CrossRef]
21. Jamali, A.; Roy, S.K.; Ghamisi, P. WetMapFormer: A unified deep CNN and vision transformer for complex wetland mapping. *Int. J. Appl. Earth Obs. Geoinf.* **2023**, *120*, 103333. [CrossRef]
22. Broni-Bediako, C.; Murata, Y.; Mormille, L.H.B.; Atsumi, M. Searching for CNN Architectures for Remote Sensing Scene Classification. *IEEE Trans. Geosci. Remote Sens.* **2022**, *60*, 4701813. [CrossRef]
23. Shawky, O.A.; Hagag, A.; El-Dahshan, E.-S.A.; Ismail, M.A. Remote sensing image scene classification using CNN-MLP with data augmentation. *Optik* **2020**, *221*, 165356. [CrossRef]
24. Li, Y.; Wang, W.; Wang, G.; Tan, Q. Actual evapotranspiration estimation over the Tuojiang River Basin based on a hybrid CNN-RF model. *J. Hydrol.* **2022**, *610*, 127788. [CrossRef]
25. Zhang, Y.-M.; Wang, H. Multi-head attention-based probabilistic CNN-BiLSTM for day-ahead wind speed forecasting. *Energy* **2023**, *278*, 127865. [CrossRef]
26. Mountrakis, G.; Heydari, S.S. Harvesting the Landsat archive for land cover land use classification using deep neural networks: Comparison with traditional classifiers and multi-sensor benefits. *ISPRS J. Photogramm. Remote Sens.* **2023**, *200*, 106–119. [CrossRef]
27. Wang, J.; Wang, P.; Tian, H.; Tansey, K.; Liu, J.; Quan, W. A deep learning framework combining CNN and GRU for improving wheat yield estimates using time series remotely sensed multi-variables. *Comput. Electron. Agric.* **2023**, *206*, 107705. [CrossRef]
28. Duan, Z.; Chu, S.; Cheng, L.; Ji, C.; Li, M.; Shen, W. Satellite-derived bathymetry using Landsat-8 and Sentinel-2A images: Assessment of atmospheric correction algorithms and depth derivation models in shallow waters. *Opt. Express* **2022**, *30*, 3238–3261. [CrossRef]
29. Roy, D.P.; Li, J.; Zhang, H.K.; Yan, L. Best practices for the reprojection and resampling of Sentinel-2 Multi Spectral Instrument Level 1C data. *Remote Sens. Lett.* **2016**, *7*, 1023–1032. [CrossRef]
30. Waldeland, A.U.; Due Trier, Ø.; Salberg, A.-B. Forest mapping and monitoring in Africa using Sentinel-2 data and deep learning. *Int. J. Appl. Earth Obs. Geoinf.* **2022**, *111*, 102840. [CrossRef]
31. Feng, T.; Duncanson, L.; Montesano, P.; Hancock, S.; Minor, D.; Guenther, E.; Neuenschwander, A. A systematic evaluation of multi-resolution ICESat-2 ATL08 terrain and canopy heights in boreal forests. *Remote Sens. Environ.* **2023**, *291*, 113570. [CrossRef]
32. Zhu, X.X.; Tuia, D.; Mou, L.; Xia, G.-S.; Zhang, L.; Xu, F.; Fraundorfer, F. Deep Learning in Remote Sensing. *IEEE Geosci. Remote Sens. Mag.* **2017**, *5*, 8–36. [CrossRef]
33. Myles, A.J.; Feudale, R.N.; Liu, Y.; Woody, N.A.; Brown, S.D. An introduction to decision tree modeling. *J. Chemom.* **2004**, *18*, 275–285. [CrossRef]
34. Zhang, L.; Wu, K.; Zhong, Y.; Li, P. A new sub-pixel mapping algorithm based on a BP neural network with an observation model. *Neurocomputing* **2008**, *71*, 2046–2054. [CrossRef]
35. Seeger, M. Gaussian processes for machine learning. *Int. J. Neural Syst.* **2004**, *14*, 69–106. [CrossRef]
36. Leonardi, N.; Canestrelli, A.; Sun, T.; Fagherazzi, S. Effect of tides on mouth bar morphology and hydrodynamics. *J. Geophys. Res. Ocean.* **2013**, *118*, 4169–4183. [CrossRef]
37. Masashi, W.; Kazuhisa, G.; Volker, R.; Fumihiko, I. Identification of Coastal Sand Deposits From Tsunamis and Storm Waves Based on Numerical Computations. *J. Geophys. Res. Earth Surf.* **2021**, *126*, e2021JF006092.
38. Li, M.; Wu, S.; Gong, X.; Yang, L.; Gou, F.; Li, J. Characteristics of coastline change under the influence of human activities in central Jiangsu Province from 1989 to 2019. *Mar. Sci.* **2022**, *46*, 60–68.
39. Wang, Y.; Liu, Y.; Jin, S.; Sun, C.; Wei, X. Evolution of the topography of tidal flats and sandbanks along the Jiangsu coast from 1973 to 2016 observed from satellites. *ISPRS J. Photogramm. Remote Sens.* **2019**, *150*, 27–43. [CrossRef]
40. Gong, Z.; Wang, Z.B.; Stive, M.J.F.; Zhang, C.K. Tidal Flat Evolution at the Central Jiangsu Coast, China. In Proceedings of the 6th International Conference on Asian and Pacific Coasts (APAC), Hong Kong, China, 14–16 December 2011.
41. Li, Z.; Wang, Z.; Zhang, K. Relationship between morphology of typical sand bars and river channels. *J. Sediment Res.* **2012**, 68–73.
42. Tao, J.; Wang, Z.B.; Zhou, Z.; Xu, F.; Zhang, C.; Stive, M.J.F. A Morphodynamic Modeling Study on the Formation of the Large-Scale Radial Sand Ridges in the Southern Yellow Sea. *J. Geophys. Res. Earth Surf.* **2019**, *124*, 1742–1761. [CrossRef]
43. Gong, Z.; Jin, C.; Zhang, C.; Zhou, Z.; Zhang, Q.; Li, H. Temporal and spatial morphological variations along a cross-shore intertidal profile, Jiangsu, China. *Cont. Shelf Res.* **2017**, *144*, 1–9. [CrossRef]